Microcellular foaming of poly(phenylene sulfide)/poly(ether sulfones) blends using supercritical carbon dioxide

Zhonglei Ma, Guangcheng Zhang, Xuetao Shi, Quan Yang, Jiantong Li, Yang Liu, Xiaolong Fan

Department of Applied Chemistry, MOE Key Lab of Applied Physics and Chemistry in Space, School of Science, Northwestern Polytechnical University, Xi'an 710072, People's Republic of China

Correspondence to: G. Zhang (E-mail: zhangguc@nwpu.edu.cn) and Z. Ma (E-mail: mazl@mail.nwpu.edu.cn)

ABSTRACT: Microcellular foaming of poly(phenylene sulfide)/poly(ether sulfones) (PPS/PES) blends presents a promising approach to produce high-performance cellular materials with tailored microstructures and enhanced properties. This study investigated the effects of multiphase blend composition and process conditions on the foaming behaviors and final cellular morphology, as well as the dynamic mechanical properties of the solid and microcellular foamed PPS/PES blends. The microcellular materials were prepared via a batch-foam processing, using the environment-friendly supercritical CO_2 (scCO_2) as a blowing agent. The saturation and desorption behaviors of CO_2 in PPS/PES blends for various blend ratios (10 : 0, 8 : 2, 6 : 4, 5 : 5, 4 : 6, 2 : 8, and 0 : 10) were also elaborately discussed. The experimental results indicated that the foaming behaviors of PPS/PES blends are closely related to the blend morphology, crystallinity, and the mass-transfer rate of the CO_2 in each polymer phase. The mechanisms for the foaming behaviors of PPS/PES blends have been illustrated by establishing theoretical models. © 2015 Wiley Periodicals, Inc. J. Appl. Polym. Sci. **2015**, *132*, 42634.

INTRODUCTION

Polymer blending is an effective, practical, and economic way of obtaining new materials with desired microstructures and properties.[1] Compared with individual polymers, the blends usually exhibit superior comprehensive properties such as impact toughness, ductility, processability, and cost effectiveness.[2] These properties of polymer blends depend greatly on the matrix properties, phase morphology, and interfacial interaction. Poly(phenylene sulfide) (PPS) is a high-performance engineering thermoplastic with superior physical and chemical properties including good melt fluidity, outstanding temperature, and chemical resistance, as well as good electrical properties. However, PPS has a poor impact toughness due to the rigid backbone chain and high crystallinity, which significantly limits its uses in many applications.[3] Blending with other toughened polymers such as poly(ether ether ketone) (PEEK),[2] polyamide 66 (PA66),[4] poly(ether imide) (PEI),[5] poly(butylene terephthalate) (PBT),[6] and ethylene copolymers[7] is a very effective method to further improve the physical and mechanical properties, especially the impact toughness of PPS. Poly(ether sulfone) (PES) is an amorphous high-performance engineering plastic with excellent thermal (high glass transition temperature) and mechanical (impact strength) properties. Thus blending PPS with PES is an important way to improve the toughness and

impact strength of PPS resin.[8] Shibata and Yosomiya[9] investigated the crystallization and melting behaviors of PPS in blends with PES prepared by melt-mixing. They found that PPS and PES have some compatibility, and the degree of crystallinity decreased with the increase of PES content.

Recently, the microcellular foaming technique has been applied to multiphase polymer systems such as semicrystalline polymers,[10–12] polymer nanocomposites,[13–17] and polymer blends[18–20] to create novel lightweight cellular materials with tailored microstructures and unique properties. Microcellular foams generally refer to foamed plastics characterized by cell sizes smaller than 10 μm and cell densities larger than 10^9 cells/cm^3.[21] Compared with solid polymers, microcellular foams exhibit many advantages including improved impact toughness, higher specific strength, lower dielectric constant and thermal conductivity, as well as reduced cost and material weight.[22,23] These unique properties enable microcellular foams to attract extensive attention for potential applications in automobile and aerospace industry, thermal and electrical insulators, packaging and filtration membranes.[24,25] Many studies have demonstrated the feasibility of developing microcellular structures in various polymer blends, that is, poly(propylene)/poly(ethylene) (PP/PE),[26,27] poly(propylene)/poly(butylenesterephthalate) (PP/PBT),[28] poly(etherimide)/poly(propylene) (PEI/PP),[29,30] and

poly(3-hydroxybutyrate-co-3-hydroxyvalerate)/poly (butylene adipate-co-terephthalate) (PHBV/PBAT).[31] Mark et al.[32] have successfully prepared the microcellular foamed poly(sulfone)/poly(benzimidazole) (PSF/PBI) blends with bimodal cell size distributions using the batch foaming technique. Open or partially open-cell structures were also successfully fabricated from these high-temperature polymer blends. Krause and Diekmann[33] studied the solid-state foaming behavior of miscible, amorphous, and high-performance poly(sulfone)/poly(imide) (PSU/PI) blends. They found that the carbon dioxide concentration and the foaming temperature are two crucial factors determining the transition from microcellular close-celled to nanoporous open-celled foams. The mechanism for microcellular foaming of the multiphase or multicomponent systems is very complex. To the best knowledge of the authors, no effort has yet been reported on the gaseous mass-transfer and microcellular foaming behaviors, as well as the final morphologies of the high-performance PPS/PES blends in the solid-state batch foaming process. Microcellular foams from the PPS/PES blends possess a large number of potential applications in the fields of aerospace and automobile industry, thermal and electrical insulators, which need high mechanical properties and heat resistance to satisfy the high-tech requirements.

Supercritical carbon dioxide ($scCO_2$) represents a particularly attractive alternative to ozone-depleting blowing agents as an efficient physical-blowing agent for the preparation of microcellular foams.[34] The gas-like diffusivity and liquid-like density of $scCO_2$ lead to high diffusion and solubility in most polymers.[35] Moreover, carbon dioxide is environmentally friendly, inexpensive, and has moderate critical conditions ($T_c = 31.3°C$, $P_c = 7.38$ MPa).[36,37] The reduction in glass transition temperature (T_g) and viscosity of polymers due to the plasticization effect of $scCO_2$ makes it very beneficial to the microcellular foaming process.[38] Nemoto and Takagi[39] reported the preparation of microcellular and nanocellular foams from poly(ether ether ketone) (PEEK)/para-dia-mine poly(ether imide) (p-PEI) as well as PEEK/meta-diamine poly(ether imide) (m-PEI) blends by a temperature quench foaming method with $scCO_2$. They found that the difference in chemical configuration between m- and p-PEI results in a prominent change in the highly ordered blend morphology and cellular structure of the respective foams. In addition, foams can provide the higher reflection ratios over the solid polymers. Siripurapu et al.[40] investigated the microcellular extrusion molding of poly(methyl methacrylate)/poly(vinylidene fluoride) (PMMA/PVDF) blends using $scCO_2$ as a blowing agent. The results demonstrated that PMMA acts as a beneficial blend partner to significantly enhance the foam homogeneity and reduce the cell size due to the increased gas solubility, improved melt-rheological behavior and suppression of the melting point.

The main objective of this study is to investigate the microcellular foaming behaviors of PPS/PES blends using the solid-state batch foaming technique with supercritical CO_2 as a physical-blowing agent. The effects of blend composition, phase morphology, and foaming conditions on the foaming behavior and final foam morphology, as well as the dynamic mechanical properties of the solid and microcellular PPS/PES blends were

systematically investigated. The phase morphology and thermal properties of the solid PPS/PES blends, and the saturation and desorption behaviors of CO_2 as functions of the blend composition were also elaborately discussed. The theoretical models for the microcellular foaming behaviors of PPS/PES blends were established to gain a fundamental understanding of the complex processing-structure-property relations.

EXPERIMENTAL

Materials

The PPS used in this study was the non-cured commercial product HB ($\overline{M}_w$=48,000), supplied by Deyang Chemical (Sichuan, China). PES was purchased from Jida Special Plastic Engineering Research. Both materials were used as received in pellet form. Carbon dioxide (CO_2) was supplied by Changte Airproduct with a purity higher than 99.99%.

Preparation of PPS/PES Blends

The PPS and PES pellets were first treated in a vacuum oven at 120°C for 6 h to remove the low molecular weight species, and then compounded using a twin-screw extruder (SHJ-95, Lantai Plastics Machinery, Lanzhou, China). The strand leaving the extruder was quenched in a water bath, pelletized, and dried in an oven at 100°C for 4 h. The dried pellets were then extruded into 1.5-mm thick PPS/PES blend sheets for gaseous mass-transfer and microcellular foaming studies using a HAAKE PolyLab OS system (Thermo Fischer Scientific, Karlsruhe, Germany). The processing temperatures of PPS/PES blends with weight ratios of 10 : 0, 8 : 2, 6 : 4, 5 : 5, 4 : 6, 2 : 8, and 0 : 10 were set as 300, 305, 310, 320, 330, 340, and 350°C, respectively, to obtain qualified PPS/PES sheets for the gaseous mass-transfer and microcellular foaming studies.

Gas Saturation and Desorption

The PPS/PES blend sheets were cut into 60 mm × 30 mm pieces and placed in a high-pressure vessel under a prescribed temperature of 45°C. Thereafter, the vessel was flushed with low-pressure carbon dioxide for about 2 min to rule out the impurities inside. The high-purity carbon dioxide was subsequently delivered to the high-pressure vessel by a supercritical fluid pump (SSI, S10SNXP1), reaching a pressure higher than the critical pressure (7.38 MPa). After a length of saturation time, the samples were removed from the autoclave and weighed on a balance (AUW120D, sensitivity 0.01 mg) to measure gas uptake.

For desorption experiments, the completely saturated samples were allowed to desorb at atmospheric conditions. Periodic mass measurements were conducted to record the amount of gas dissolved in the PPS/PES blends. Generally, it took 30 s during the removing and weighing processes before the first data was recorded. These data points were used to evaluate the desorption diffusivities for the PPS/PES blends with various blend ratios. For short desorption time, the desorption behaviors can be described using the Fickian diffusion equation:[41]

$$M_d = M_\infty - \frac{4M_\infty}{l}\sqrt{\frac{D_d t_d}{\pi}} \qquad (1)$$

where M_d refers to the amount of gas dissolved in the samples at desorption time t_d, expressed as the weight percentage of

CO_2 per unit weight of PPS/PES blends. M_∞ refers to the total sorption amount of gas that has saturated for a sufficiently long time and simultaneously the amount of gas at the beginning of the desorption. According to eq. (1), a plot of M_d versus the square root of desorption time, $t_d^{1/2}$, should be linear. M_∞ was obtained by extrapolating the residual gas amount M_d to the zero desorption time. Thus the diffusivities of desorption, D_d, could be calculated from the slopes of the plot and the values of M_∞ using the following equation:

$$D_d = \frac{\pi}{16}\left(\frac{l}{M_\infty}\right)^2\left(\frac{\Delta M_d}{\Delta\sqrt{t_d}}\right)^2 \qquad (2)$$

Microcellular Foaming Procedure

Specimens were saturated with $scCO_2$ at a constant temperature of 45°C and at moderate pressures (8, 12, and 16 MPa in this study) for at least 12 h to get completely saturated. Subsequently, the CO_2 was rapidly released from the autoclave with a depressurization rate higher than 0.6 MPa/s. After removing the PPS/PES sheets from the high-pressure vessel, the samples were immersed in a silicon oil bath maintained at the prescribed foaming temperatures. To remove the excess oil from the surface of the samples, the microcellular foamed PPS/PES blends were immediately quenched in an ethanol/water mixture, washed for half an hour, and dried under vacuum at 30°C for 24 h.

Material Characterizations

Differential Scanning Calorimetry (DSC). Thermal properties of the PPS/PES blends were measured using a differential scanning calorimeter (DSC1, Mettler Toledo, Switzerland). During DSC tests, a thermal scanning range from 25 to 320°C with heating rate of 10°C/min was applied. The glass transition temperature (T_g) of PES, enthalpy of cold crystallization (ΔH_c), and apparent melting enthalpy (ΔH_f) of PPS were determined from the heating curves.

Crystallinity of the PPS phase was calculated by

$$\chi_c(\%\text{ crystallinity}) = \frac{\Delta H_f - \Delta H_c}{\Delta H^0 \cdot W} \times 100\% \qquad (3)$$

where ΔH^0 is the enthalpy of melting per gram of 100% crystallinity (perfect crystal) of PPS (80.75 J/g)[42], and W is the weight fraction of PPS phase in the blends.

Wide-Angle X-ray Diffraction (WAXD). Wide-angle X-ray diffraction experiments were conducted on a Philips X'Pert Pro X-ray diffractometer at 40 kV and 200 mA with a scanning rate of 2°/min. It should be noted that the samples prepared for the WAXD measurements experienced the similar thermal history as those for the thermal property studies by DSC mentioned earlier.

Scanning Electron Microscope (SEM). The morphologies of the solid and microcellular PPS/PES blends were investigated using a TESCAN (VEGA 3 LMH) scanning electron microscope (SEM). The samples were freeze fractured in liquid nitrogen and sputter coated with Au/Pd. Etching experiments were conducted by dipping the samples into dimethyl sulfoxide (DMSO) and vibrating in an ultrasonic washer with the frequency of 100 Hz for 90 min. Image analysis on the SEM photographs was conducted using the software Image-Pro Plus to obtain the

average cell size and cell density. The average cell diameter was determined by taking average cell diameters of at least 200 cells from the data of SEM observation. The cell density N_f was calculated using the following equation[43]

$$N_f = \left[\frac{nM^2}{A}\right]^{3/2} \qquad (4)$$

where n is the number of cells, A is the area of the micrograph in cm^2, and M is the magnification factor.

Dynamic Mechanical Analysis (DMA). Dynamical mechanical analysis (DMA) was performed on a TA instruments analyzer (model Q800) in single cantilever mode. Rectangular specimens were tested at a frequency of 1 Hz with a heating rate of 5°C/min. The values of storage modulus (E') and loss factor ($\tan\delta$) were provided by the dynamic tests.

RESULTS AND DISCUSSION

Morphology of Solid PPS/PES Blends

The fracture characteristics of solid PPS, PES, and PPS/PES blends were investigated by SEM technology, and the results are shown in Figure 1(a). It can be seen that the pure PES shows a typical fracture surface of an amorphous polymer without visible plastic deformation, whereas the pure PPS shows an irregular fracture feature because of its crystalline structure and more brittle fracture behavior. The PPS/PES blends exhibit a typical surface morphology of a partial miscible system that has good interfacial bonding, and no obvious phase separation can be seen. Figure 1(b) shows the fracture surfaces of PPS, PES, and PPS/PES blends chemically extracted by the DMSO at room temperature for 40 h as the PES phase can be easily dissolved. The morphology of PPS/PES blends changes from the single continuous phase structure to the bicontinuous phase structure as the PES increases. The PPS/PES blends with weight ratios higher than 2 : 8 present a sea-island morphology. It is noted that PPS exists as the continuous phase in the whole ratio range of PPS/PES blends due to its good melt flowability.

Thermal Properties

Figure 2 shows the DSC representative thermograms of PPS, PES, and PPS/PES blends obtained from the heating scans. Table I summarizes the numerical values of temperature and enthalpy, as well as the degree of crystallinity for the PPS phase. Pure PES is in the amorphous state and the glass-transition behavior can be differentiated from the DSC heating curve. For the pure PPS, no obvious glass-transition behavior is observed in the curves due to the high crystallinity (51.50%) and thereby it's not applicable to determine a defined glass transition temperature. With increasing PPS content, the glass transition temperature of PES phase shifts to lower temperature, demonstrating that the PPS and PES are partial miscible. The melting enthalpy ΔH_f and the crystallinity of the PPS phase decrease as the PES content increases. This is mainly because that the incorporation of PES destroys the continuity and decreases the crystalline ability of PPS phase, leading to a reduced crystallinity.
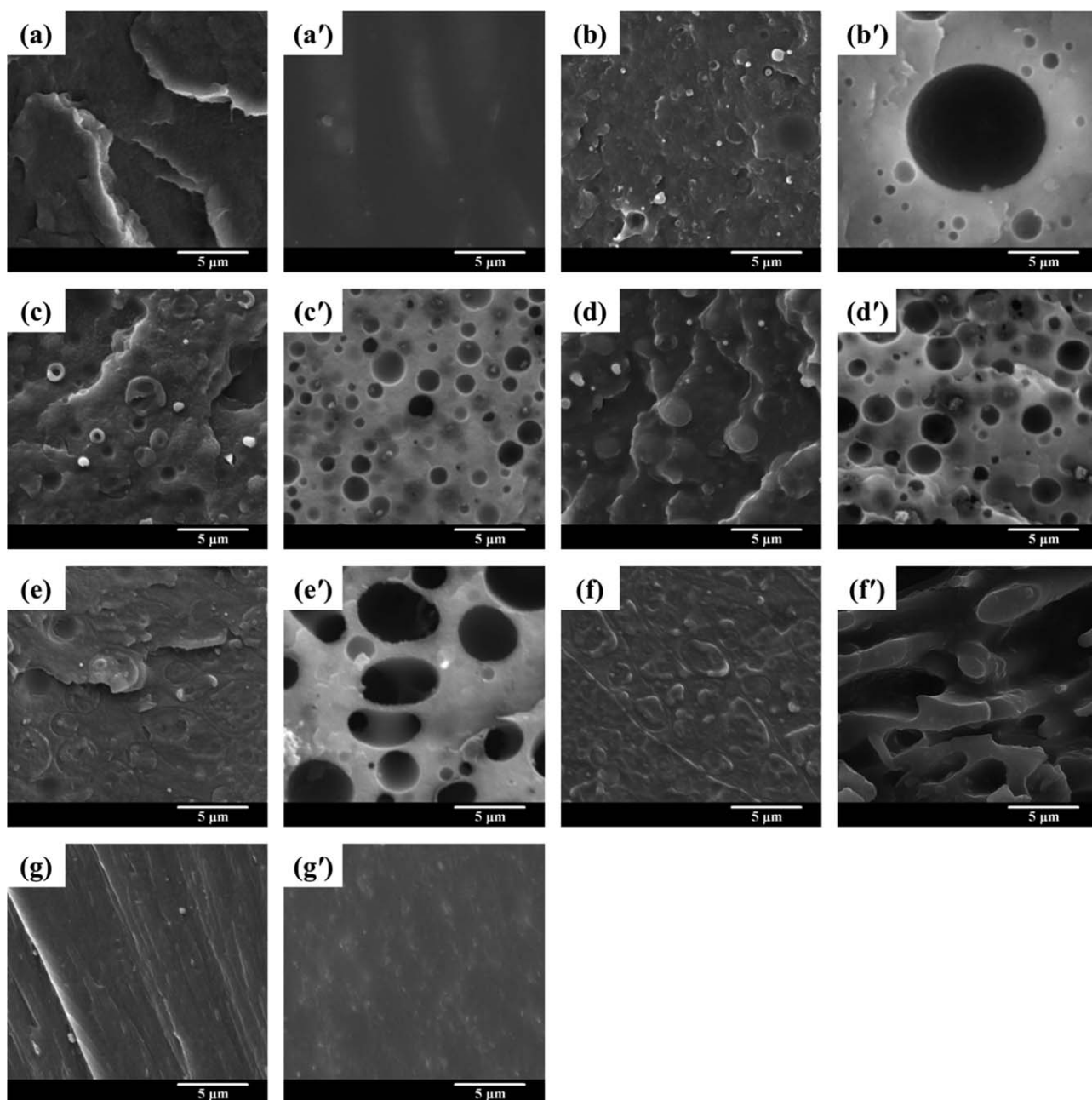
Figure 1. SEM micrographs of PPS, PES, and PPS/PES blends: (a) 10 : 0, (b) 8 : 2, (c) 6 : 4, (d) 5 : 5, (e) 4 : 6, (f) 2 : 8, (g) 0 : 10. SEM micrographs of PPS, PES, and PPS/PES blends extracted by the dimethyl sulfoxide (DMSO): (a′) 10 : 0, (b′) 8 : 2, (c′) 6 : 4, (d′) 5 : 5, (e′) 4 : 6, (f′) 2 : 8, (g′) 0 : 10.

Wide-Angle X-ray Diffraction (WAXD)

The effects of blend composition on the crystalline structure of PPS/PES blends were investigated. Figure 3 shows the WAXD patterns of PPS, PES, and PPS/PES blends. As can be seen, the pure PPS and PPS-rich blends have a strong crystalline ability, and exhibit diffraction peaks at $2\theta = 18.78°$, $20.39°$, $25.38°$, and $27.24°$. The PES is an amorphous polymer exhibiting a weak and broad peak. With increasing PES content, the diffraction intensity of peaks significantly reduces. It is noted that at a low blend ratio of 2 : 8, the curve of PPS/PES blends shows a distinct diffraction peak of PPS at $2\theta = 20.39°$. This is due to that the excellent melt fluidity of PPS results in a continuous phase

even at low PPS content (20%) and thereby crystal structure can be formed in the PPS phase. However, the continuity of PPS phase has been destroyed to some extent by the PES phase with a large PES content, thus the diffraction peak of PPS/PES(2 : 8) blends at $2\theta = 20.39°$ is much weaker than that of PPS/PES(4 : 6) blends.

Gas Saturation and Desorption

The gaseous mass-transfer behaviors of the PPS/PES blends including gas saturation and desorption processes were investigated under a wide range of processing conditions. Figure 4(a) shows the absorbed amount of carbon dioxide in units of mg
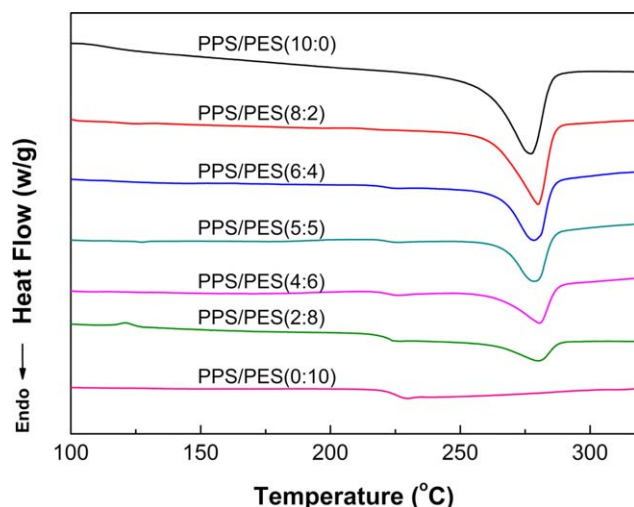
Figure 2. DSC curves of PPS, PES, and PPS/PES blends at a heating rate of 10°C/min. [Color figure can be viewed in the online issue, which is available at wileyonlinelibrary.com.]
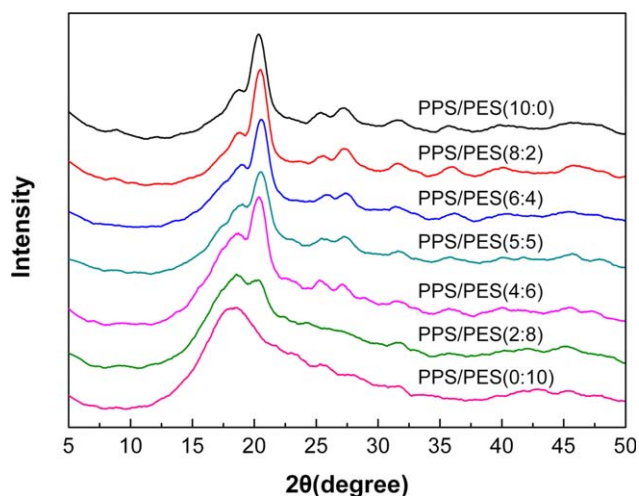

Figure 3. WAXD patterns of PPS, PES, and PPS/PES blends. [Color figure can be viewed in the online issue, which is available at wileyonlinelibrary. com.]

CO_2 per gram of PPS/PES blends as a function of saturation time at 45°C. As can be seen, the gas concentration in the PPS/ PES blends increases and then reaches equilibrium with the increasing saturation time. The time needed to reach equilibrium concentration increases significantly as the PPS content increases. This is because that the highly crystalline PPS component has a low gas diffusion and solubility. Moreover, the diffusion path in the PPS component is altered when the CO_2 molecules meet the spherulite barriers, leading to an increased length of diffusion path and a reduced diffusion rate. Figure 4(b) shows the plots of the equilibrium concentration as a function of the PPS/PES ratio at three saturation pressures of 8, 12, and 16 MPa. All the samples were placed in the autoclave for 12 h in order to get completely saturated. It can be seen that the equilibrium gas concentration increases with the increasing PES content and saturation pressure. In addition, the gas concentration in the PPS/PES blends is much lower than the pure PES.

Figure 5 shows the desorption curves of CO_2 in the pure PPS, PES, and PPS/PES blends saturated at 12 MPa and 45°C for 12 h. The dissolved gas escapes from the sheet surface and the gas concentration decreases with the increasing desorption time t_d. It is found that the desorption curves of all blends are not

Table I. Thermal Characteristics of the PPS/PES Blends Obtained from the Heating DSC Curves

PPS/PES	T_g(PES) (°C)	ΔH_f (PPS)(J/g)	χ(PPS) (%)
10 : 0	—	41.59	51.50
8 : 2	209.02	32.65	50.54
6 : 4	216.32	24.05	49.64
5 : 5	216.40	18.69	46.29
4 : 6	216.65	14.70	45.51
2 : 8	217.37	7.16	44.33
0 : 10	220	—	—

linear, indicating that the desorption kinetics of blends does not meet the Fickian law in the present desorption time scope. According to eq. (2), however, the desorption diffusivities of CO_2 can be evaluated using the linear fitting of the curves at a short desorption time. The calculated D_d values for different PPS/PES blend ratios are presented in Table II. As can be seen, D_d has a considerable blend ratio dependence. The increase in PES content causes the increase in the desorption diffusivity due to the higher gas diffusion rate in PES phase. The maximum D_d is 1.88×10^{-11} m²/s with the largest M_∞ of 77.90 mg CO_2/g PES, whereas the minimum D_d is 1.58×10^{-12} m²/s with the lowest M_∞ of 16.39 mg CO_2/g PPS. It is noted that the gas desorption diffusivity in PPS/PES (2 : 8) blends is much lower than that of the pure PES. This is mainly due to that the continuous crystalline PPS phase greatly prevents the diffusion of CO_2 molecules in the PPS/PES blends even at a low PPS content.

Microcellular Foaming and Cellular Structures
Morphology of Microcellular PPS/PES Blends. Figure 6 shows the morphologies of microcellular PPS, PES, and PPS/PES blends foamed at 260°C for 4 s. All the specimens were saturated in the autoclave at 45°C and 12 MPa for 12 h. It can be seen that the blend composition has a great effect on the cellular structures of the microcellular foams. The highly crystalline PPS exhibits a relatively low foaming ability due to the low gas solubility and high matrix stiffness. However, nano-sized features are found sparsely distributed in the pure PPS. By blending with the amorphous PES, the microcellular foamability of PPS is greatly improved. As shown in the SEM micrographs of PPS/PES blends, the cellular structure are mainly formed in the PES phase and at the interfaces of PPS and PES. It is believed that the interfaces between the PPS and PES phases in the partial miscible blends can serve as favorable heterogeneous nucleating sites for cell formation due to the decreased activation energy barrier. Moreover, the higher gas solubility in the PES phase must be advantageous to the microcellular foaming process. The amorphous PES exhibits a cellular structure with a
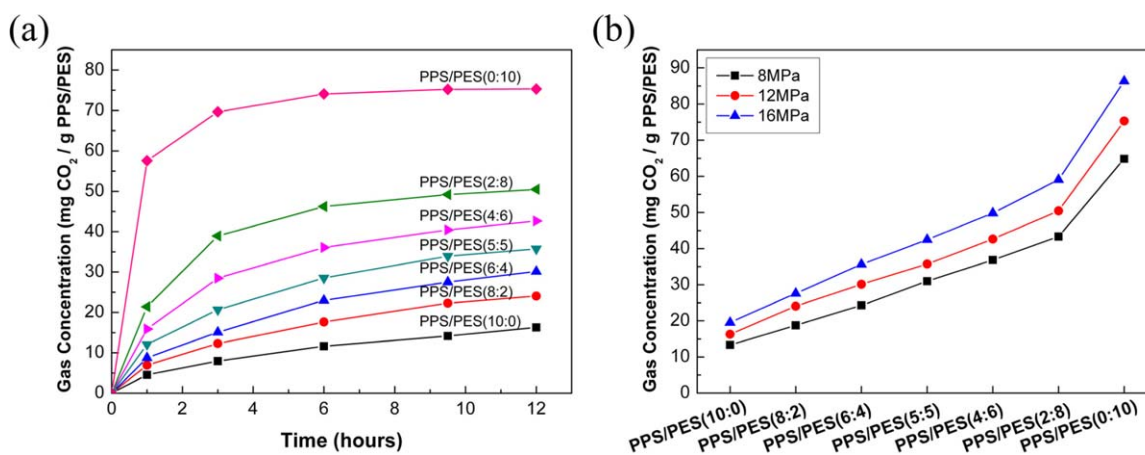
Figure 4. (a) Plots of gas concentration for PPS, PES, and PPS/PES blends as a function of saturation time. Saturation pressure: 12 MPa. (b) Equilibrium CO_2 concentration for PPS, PES, and PPS/PES blends at various saturation pressures. [Color figure can be viewed in the online issue, which is available at wileyonlinelibrary.com.]

unimodal cell-size distribution due to the homogeneous cell nucleation.

Figure 7 shows the cell morphologies of microcellular foamed PPS, PES and PPS/PES blends at an elevated foaming temperature of 300°C, which is higher than the melting temperature of PPS (278°C). As can be seen, all the foams present increased cell densities and larger expansion ratios compared to those foamed at 260°C. It is thought that the higher foaming temperature results in the decreased polymer viscosity, increased gas diffusion and cell nucleation rate. Numerous irregular cell structures are generated in the pure PPS due to the melting of crystalline regions at the higher foaming temperature. Microcellular PPS/PES (8 : 2) foams show a unique hierarchical cellular structure in which large cells embrace a foamed PES particle with open-cell structure and small cells exist around the large cells. This is different from those foamed at 260°C in which the PES particle exists inside the large cells as a sphere with smooth sur-

face. With increasing PES content, the microcellular foamed PPS/PES blends show much more uniform cellular structures.

Microcellular PPS/PES (2 : 8) foams exhibit distinctly different cellular structures in the transverse section (perpendicular to the extrusion flow direction) and the longitudinal section (parallel to the extrusion flow direction). As shown in Figure 8(b,d), stick-like PES phase is observed in the longitudinal section of microcellular foams foamed at 260 and 300°C for 4 s. This is because most of the PES phase exists in the continuous stick-like form, and the rest of the PES phase is pelletized into smaller dispersed particles under the shear force. By contrast, all the PPS phase exists in the continuous form due to its good melt fluidity. During the foaming process, obvious gas channels and spherical cells are generated around the stick-like PES and the PES particles, respectively. As the foaming temperature increases from 260 to 300°C, the size of the spherical cells around PES particles increases, while that of the gas channels around stick-like PES remains almost unchanged. The expected reason is that CO_2 gas at the interfaces between the PPS matrix and stick-like PES can escape easily once the gas channels are formed. As a consequence, the foaming temperature has little effect on the cellular structures of microcellular PPS/PES (2 : 8) foams. The results of microcellular PPS/PES blends demonstrate
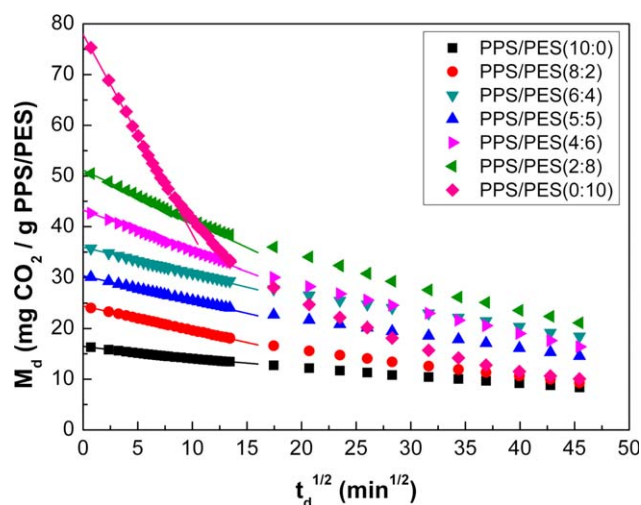

Figure 5. Plots of measured desorption weight fraction (M_d) against the square root of desorption time (t_d). [Color figure can be viewed in the online issue, which is available at wileyonlinelibrary.com.]

Table II. CO_2 Sorption Amounts and Desorption Diffusivities of PPS, PES, and PPS/PES Blends

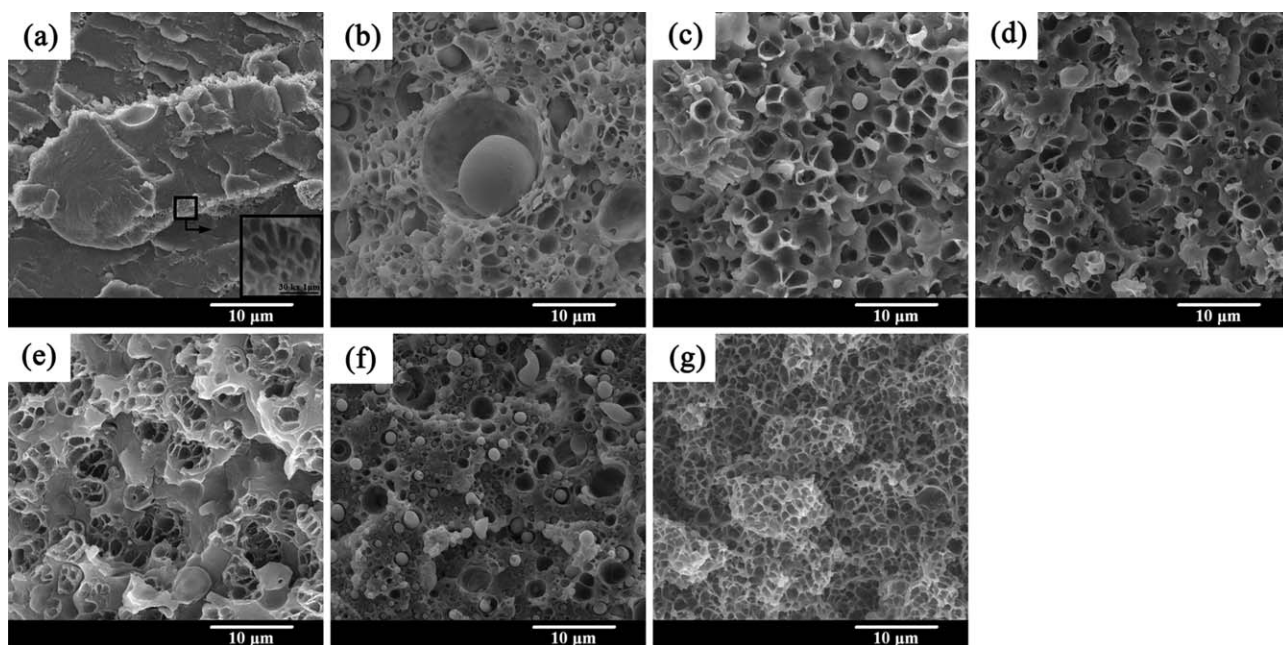| Sample	M_∞ (mg CO_2/g PPS/PES)	D_d (m²/s)
PPS/PES (10 : 0)	16.39	1.58E-12
PPS/PES (8 : 2)	24.44	1.92E-12
PPS/PES (6 : 4)	30.40	1.94E-12
PPS/PES (5 : 5)	35.95	2.22E-12
PPS/PES (4 : 6)	43.27	2.55E-12
PPS/PES (2 : 8)	51.14	2.91E-12
PPS/PES (0 : 10)	77.90	1.88E-11

Saturation condition: 12 MPa and 45°C.

Figure 6. SEM micrographs of microcellular PPS, PES, and PPS/PES blends foamed at 260°C for 4 s: (a) 10 : 0, (b) 8 : 2, (c) 6 : 4, (d) 5 : 5, (e) 4 : 6, (f) 2 : 8, (g) 0 : 10. Magnification: ×5000.

that the final cellular structures greatly depend on the blend composition and phase morphology.

Effect of Foaming Temperature and Foaming Time. The effect of foaming time on the cell morphology of microcellular PPS/PES blends foamed at two different foaming temperatures (260 and 300°C) is investigated. The saturation pressure and saturation time used are 12 MPa and 12 h, respectively. As can be seen in Figure 9(a), PPS/PES (8 : 2) blends exhibit different

foaming behaviors at the two foaming temperatures. When the foaming temperature is 260°C, cell nucleation and cell growth mainly take place at the interfaces of PPS and PES. This creates a special cellular structure, in which the large cell embraces a PES particle. The cell morphologies of microcellular PPS/PES (8 : 2) blends are very similar to that of the microcellular PEG/PS blends reported by Taki *et al.*[44] With increasing foaming time, the large cell becomes bigger and tiny holes appear on the surface of the dispersed PES phase. This result suggests that
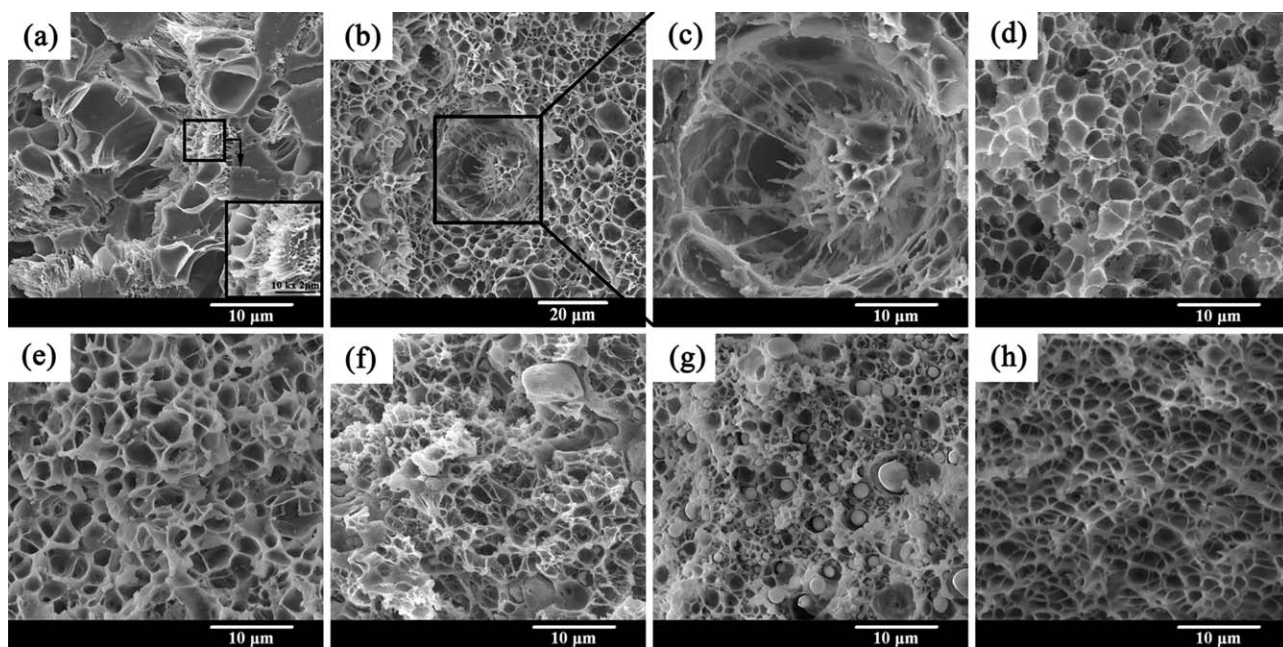

Figure 7. SEM micrographs of microcellular PPS, PES, and PPS/PES blends foamed at 300°C for 4 s: (a) 10 : 0, (b) and (c) 8 : 2, with magnifications of ×2000 and ×5000, respectively, (d) 6 : 4, (e) 5 : 5, (f) 4 : 6, (g) 2 : 8, (h) 0 : 10.
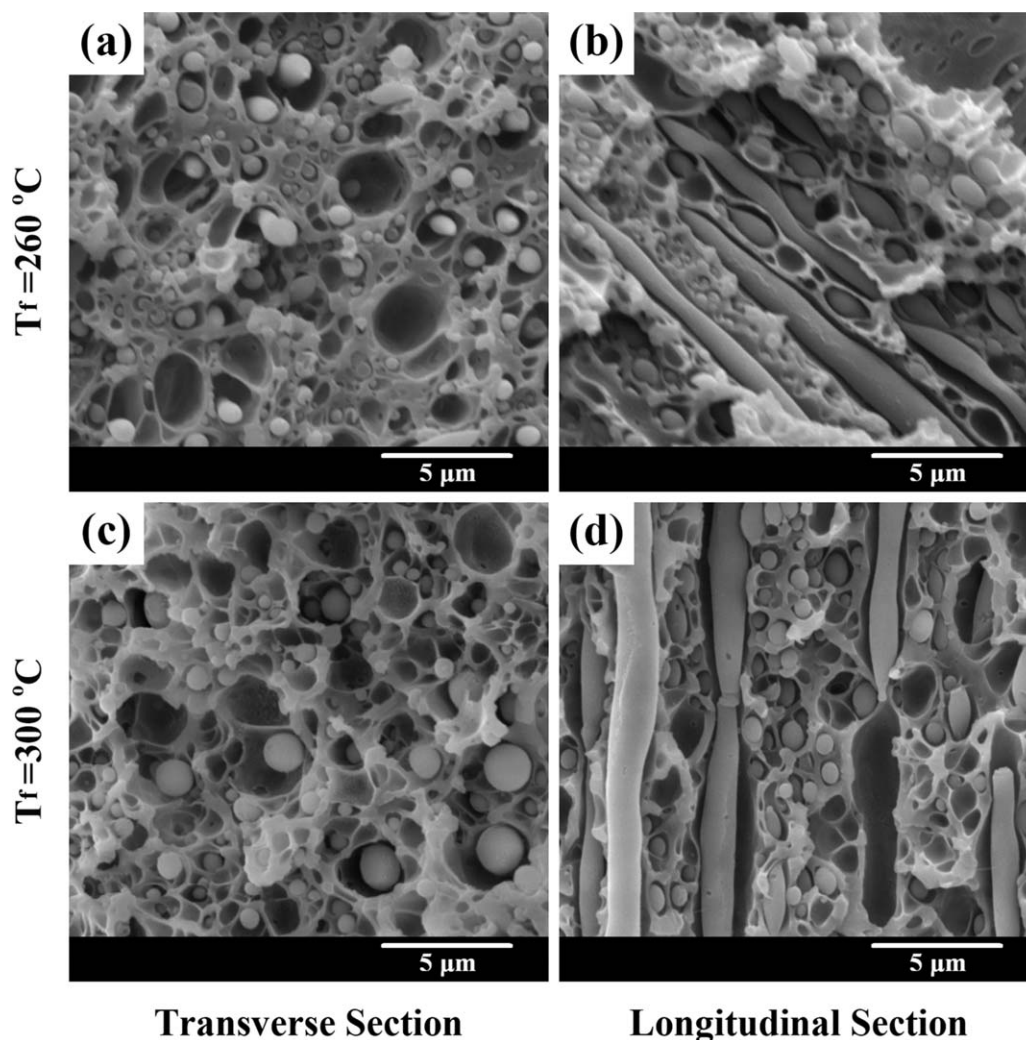
Figure 8. (a) and (b) Transverse section and longitudinal section of microcellular PPS/PES (2 : 8) foamed at 260°C, (c) and (d) Transverse section and longitudinal section of microcellular PPS/PES (2 : 8) foamed at 300°C.

microcellular structures may have been formed inside the dispersed PES spheres. Moreover, the supersaturated gas in the PES matrix has a tendency to diffuse into the large cells surrounding the particles and contribute to increased internal pressure for cell growth. When the foaming temperature is increased to 300°C, the cell nucleation and cell growth occur not only in the dispersed PES phase and at the interfaces of PPS and PES, but also in the continuous PPS phase due to the melting of crystalline regions and the reduced matrix strength. As a result, the cell density of the microcellular foams increases significantly compared to those foamed at 260°C. It is interesting to found that the dispersed PES particles have a larger foaming degree as the foaming time increases to 300°C, and the morphology changes from the microscopic porous structure to the highly open-cell structure. The filaments connecting the continuous PPS matrix and the dispersed PES particles demonstrate that the two polymer phases have a good adhesive ability at high temperatures above the melting temperature of PPS.

Figure 9(b) shows the morphology changes of microcellular PPS/PES (6 : 4) blends during the cell growth processes at 260

and 300°C. It is shown that at 260°C, the PES phase presents a confined foaming behavior due to the restriction of the strong crystalline PPS matrix. Single-hollow cells are generated in the PES phase and the cells grow in a low expansion rate. The continuous stronger PPS phase serves as template to control the cell size and location. When the foaming temperature increases to 300°C, a larger expansion of the foams appears. Homogeneous cells are generated in the PES regions and a low cell density is obtained when the foaming time is 2 s. The increased foaming time allows the melting of crystalline regions and the cell formation in the PPS phase, leading to the highly inhomogeneous cellular morphologies. The cell density increases with increasing foaming time due to the formation of microcellular structures in the PPS region, and then decreases by further increase of the foaming time because of the cell growth and cell coalescence. Figure 9(c) presents the microstructures of the microcellular PPS/PES blends with a higher PES content of 60%. The size of the dispersed phase, which is controlled by the blend composition and processing history, becomes much larger than that of the PPS/PES (6 : 4) blends. Consequently,
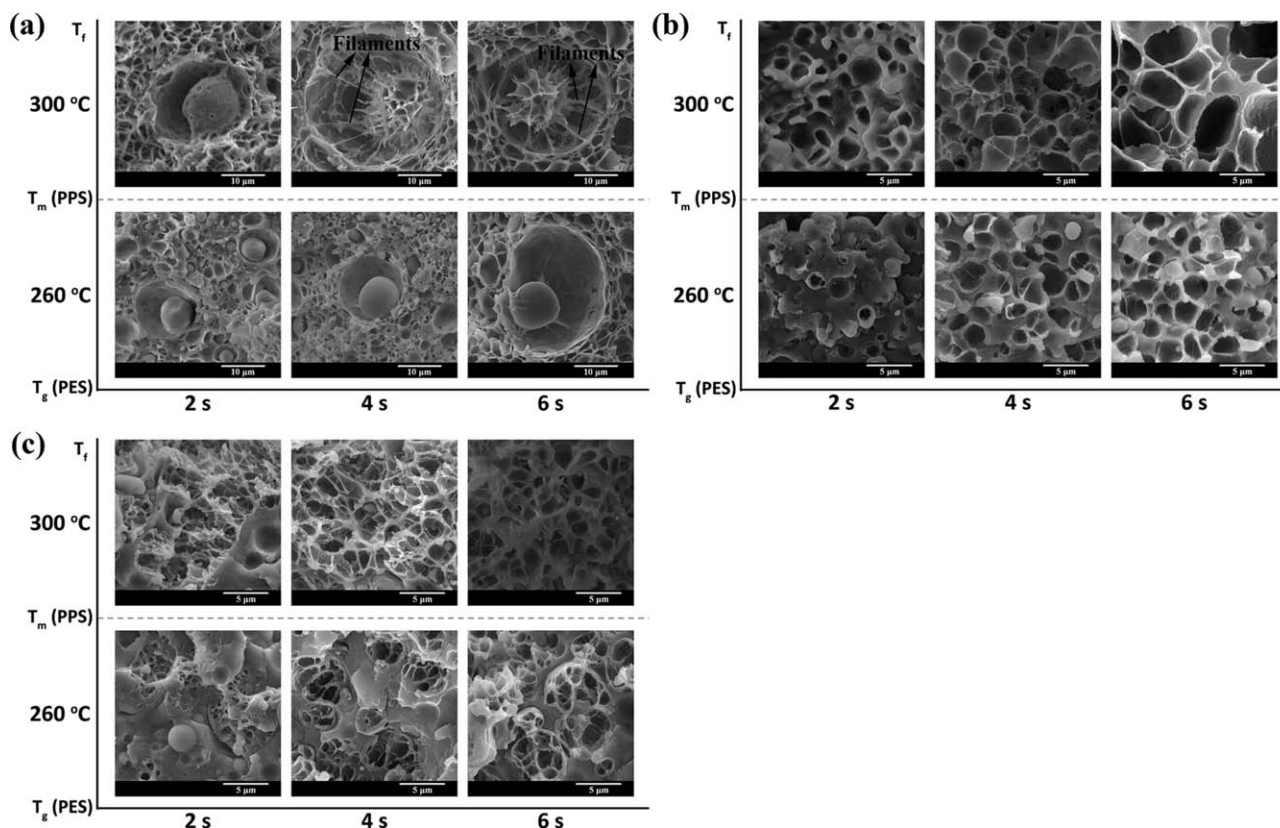
Figure 9. Morphology changes of microcellular PPS/PES blends during the cell growth process at various foaming times: (a) PPS/PES (8 : 2), (b) PPS/PES (6 : 4), and (c) PPS/PES (4 : 6). Magnification: (a) ×5000, (b) and (c) ×10,000.

numerous cell nuclei are generated in the less viscous PES matrix at the foaming temperature of 260°C. With the increasing foaming time, rapid cell growth and collapse are observed due to the high solubility and diffusivity of CO_2 in PES. At the elevated foaming temperature of 300°C, the foamed area expands with the increasing foaming time and large amounts of smaller cells are obtained throughout the volume.

Mechanisms for Microcellular Foaming Behaviors. Descriptive models are established to illustrate the microcellular foaming behaviors of PPS/PES blends with blend ratios of 8 : 2, 6 : 4, and 4 : 6. The detailed mechanism is presented in Figure 10 with the foaming time representing the cell growth process on the X-axis and foaming temperature on the Y-axis. According to the spinodal decomposition principle, gas molecules can diffuse into clusters to form spherical nuclei, or directly coalescence into a cell at a high gas concentration.[45] Compared with the PPS and PES phases, the PPS/PES interface possesses higher gas concentration and lower activation energy barrier. This results in that the cell nucleation preferentially takes place at the interface during the depressurization process.

At a low PES content of 20%, cell nucleation initially starts in the PES phase and at the interfaces of PPS and PES at both low and high foaming temperatures. The PPS and PES phases act as CO_2 reservoirs to supply CO_2 for the gas consumption at the interface. Rapid cell growth appears and cellular structures of large cells embracing open-cell PES particles are formed at the high foaming temperature, while the foaming process develops much more slowly at the low foaming temperature. At an intermediate PES content of 40%, smaller and finer dispersed PES particals are detected due to the higher extrusion temperature, leading to the generation of single-hollow cells in the PPS microspheres. The small particle size of the dispersed PES phase is supposed to restrict the formation of larger cells at the low foaming temperature. Inhomogeneous cell morphologies are observed at the high foaming temperature. When the PES content is increased to 60%, cellular structures with a regional distribution are formed by cell nucleation in the PES phase. At high foaming temperature, the discrepancy of cell morphology in the PPS and PES phases becomes much smaller due to the high foaming temperature and the sufficient CO_2 concentration for foaming. When expansion continues with the increasing foaming time, the contact between adjacent cells occurs and thus the shared wall will become thinner. Cell coalescence or rupture takes place when the cell wall gets weakened to a point. Moreover, the drainage flow would appear to accelerate cell wall thinning as a result of the pressure difference between the pressure in the cell wall and the pressure in the corner, resulting in cell breakage when the critical thickness is reached.[45]

Effect of Saturation Pressure. To investigate the saturation pressure dependence of cellular structures for PPS/PES blends, all the specimens were firstly saturated in the autoclave at the temperature of 45°C and pressures of 8, 12, and 16 MPa for 12 h. Then the completely saturated specimens were foamed at a prescribed foaming temperature of 300°C for 4 s. Figure 11
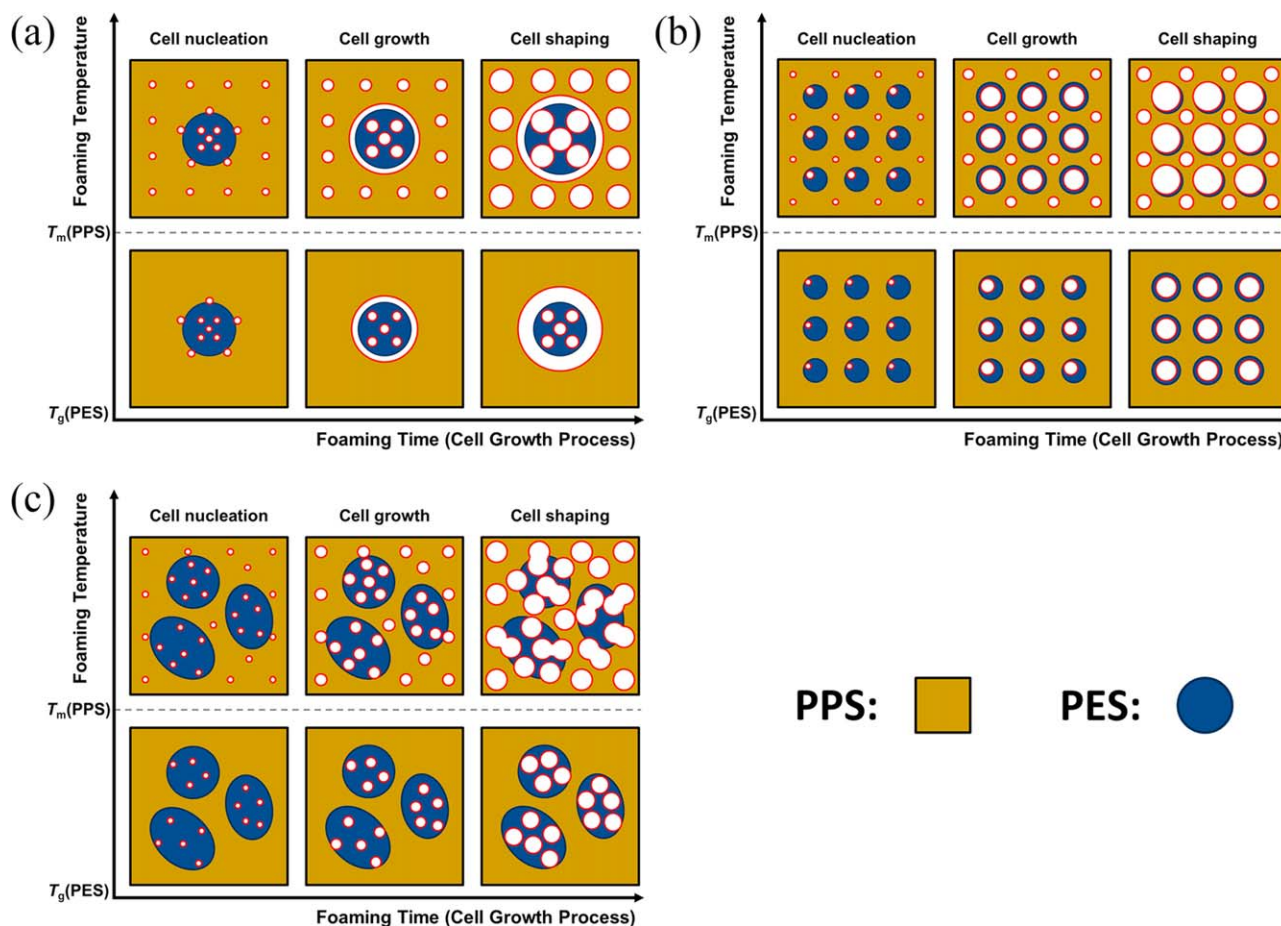
Figure 10. Mechanisms for the microcellular foaming behaviors of PPS/PES blends: (a) PPS/PES (8 : 2), (b) PPS/PES (6 : 4), and (c) PPS/PES (4 : 6). [Color figure can be viewed in the online issue, which is available at wileyonlinelibrary.com.]

shows the effect of saturation pressure on the cell morphology of microcellular PPS/PES (8 : 2) blends. As can be seen, higher saturation pressure will result in smaller cell size and larger cell density in the microcellular PPS/PES blends due to the higher gas concentration. Specifically, the energy barrier for cell nucleation decreases with the increasing pressure drop, resulting in increased number of nuclei at elevated gas pressures.[46] The single cells surrounding the dispersed PES droplets become much smaller with the increasing saturation pressure. This is due to that microcellular foaming of the amorphous PES droplets has a much stronger pressure dependence than the continuous PPS phase.

Figure 12 shows the SEM images of PPS/PES (4 : 6) blends and pure PES saturated at the three different pressures and foamed under 300°C for 4 s. As mentioned above, the PPS/PES (4 : 6) blends present a structure consisting of a continuous PPS phase and a dispersed PES phase. At a low saturation pressure of 8 MPa, the dispersed PES phase is foamed while the strong crystalline PPS phase is unfoamed. With the saturation pressure increases, the foamed area and the foaming degree become much larger. From Figure 12(d–f), the microcellular PES foams present a unimodal cell-size distribution due to the homogeneous cell nucleation. With increasing saturation pressure from 8

to 16 MPa, the cell size decreases from 1.82 to 0.92 μm, and the cell density increases from 3.68×10^{11} to 4.20×10^{12} cells/cm^3.

From the above results, it can be concluded that the blend composition and operating conditions including saturation pressure, foaming temperature and foaming time are the key factors controlling the final cellular structures of microcellular PPS/PES blends. The phase morphology of the blends depends on the ratio of the two components, and determines the foam morphology including cell size and distribution, as well as cell density. The foaming temperature plays the most important role in determining the cell nucleation and cell growth processes, as the PPS/PES blends present significantly different microcellular foaming behaviors at the temperatures below and above the melting temperature of PPS (278°C). The distinct different cellular structures can be attributed to the differences of polymer viscosity, gas diffusion and cell nucleation rate at different foaming temperatures. With the increasing foaming time, the cell size becomes much larger, and the cell coalescence and collapse take place in the microcellular PPS/PES blends. The cell nucleation and cell growth processes are much more rapid at elevated foaming temperature. Similar cellular structures can be obtained at varying saturation pressures. Nevertheless, higher saturation pressure will lead to much smaller cell size and larger cell density.
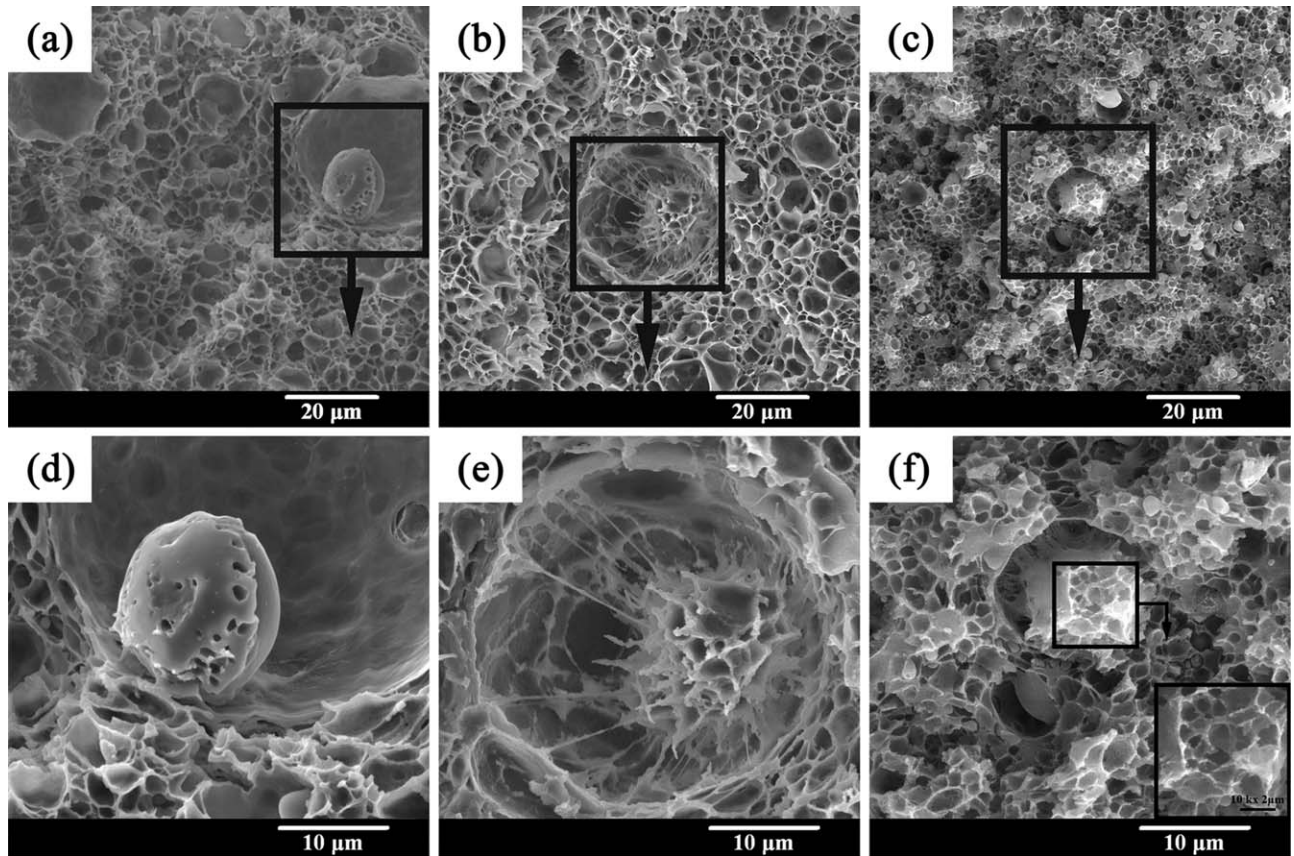
Figure 11. Effect of the saturation pressure on the morphologies of microcellular PPS/PES (8 : 2) blends: (a) and (d) 8 MPa, (b) and (e) 12 MPa, (c) and (f) 16 MPa. Magnification: (a)–(c) ×2,000, (d)–(f) ×5,000.
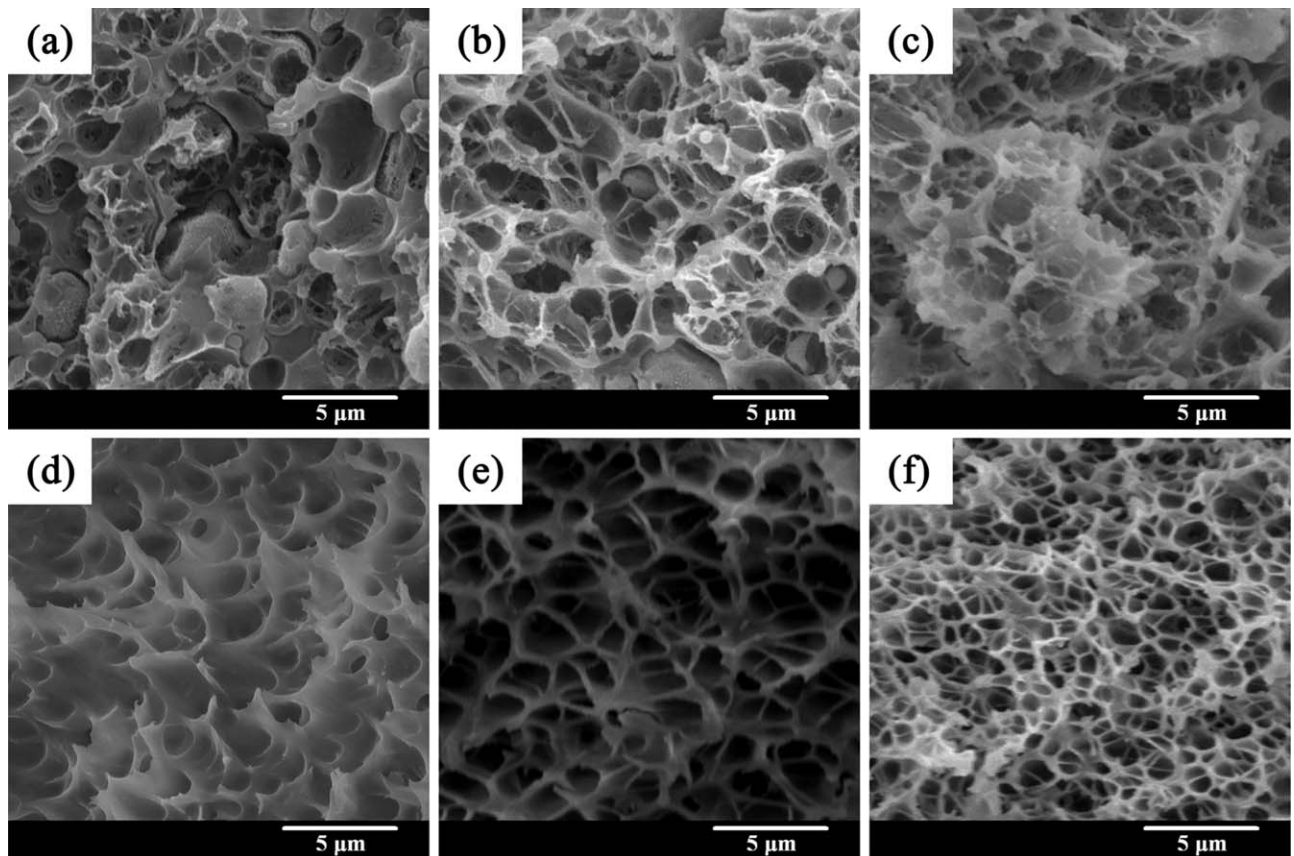

Figure 12. (a)–(c) Morphologies of microcellular PPS/PES (4 : 6) blends saturated at 8, 12, and 16 MPa, respectively; (d)–(f) Morphologies of microcellular PES foams saturated at 8, 12, and 16 MPa, respectively. Magnification: ×10,000.

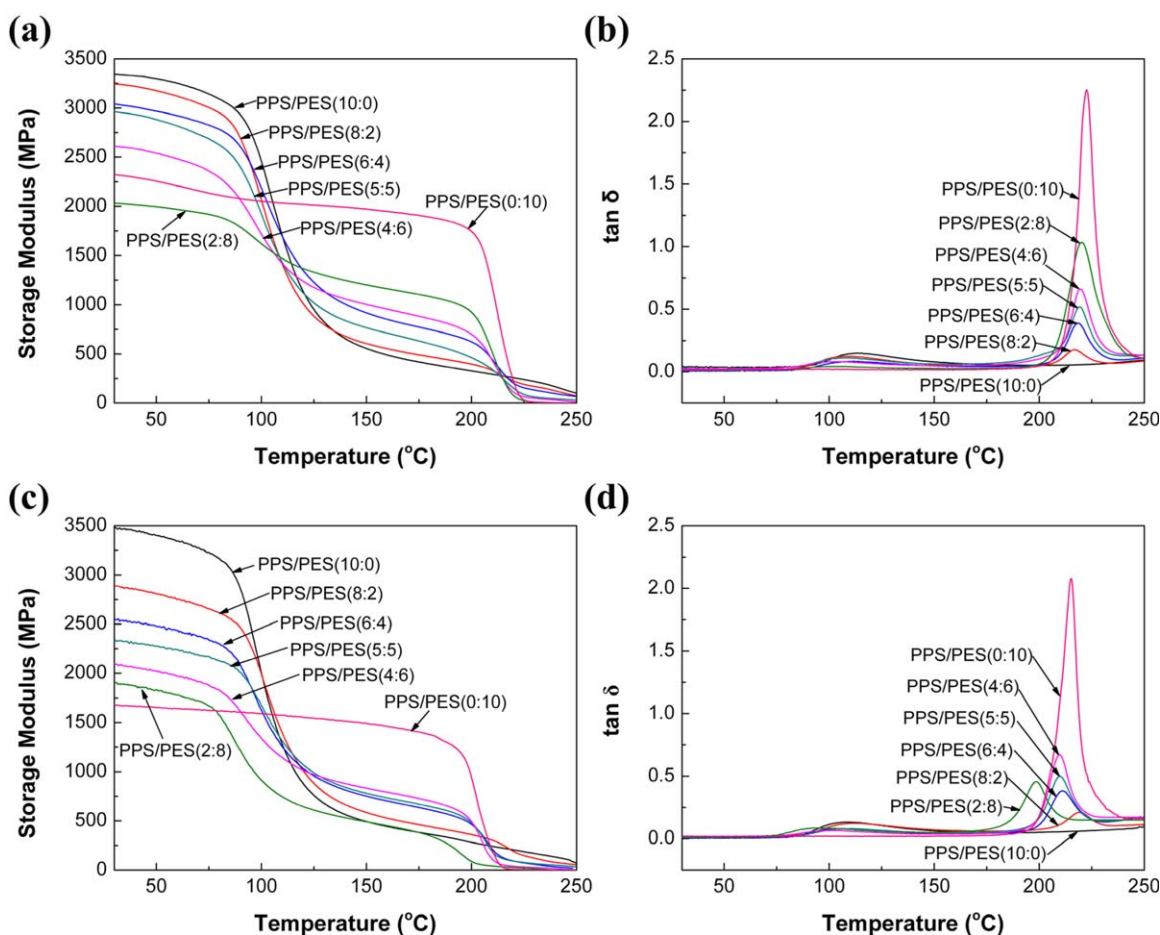**Figure 13.** Dynamic mechanical properties of the solid and microcellular PPS/PES blends: (a) and (b) storage modulus and tanδ of the solid PPS/PES blends; (c) and (d) storage modulus and tanδ of the microcellular PPS/PES blends. [Color figure can be viewed in the online issue, which is available at wileyonlinelibrary.com.]

Dynamic Mechanical Properties of Solid and Microcellular PPS/PES Blends

The viscoelastic properties of the solid PPS, PES and PPS/PES blends and the microcellular ones saturated at 12 MPa for 12 h and foamed at 260°C for 4 s were studied using DMA. From Figure 13, it can be seen that the blend ratio has significant influences on the dynamic mechanical properties including storage modulus (E') and loss factor (tanδ). The storage modulus of all solid and microcellular PPS/PES blends declines with increasing temperature, with the most rapid reduction in the glass transition regions of PPS and PES. With the increasing PES content, the storage modulus of both solid and microcellular PPS/PES blends at low temperatures decreases due to that the amorphous PES exhibits weaker elastic properties than the crystalline PPS phase. However, the storage modulus of the solid PPS/PES (2 : 8) blends is lower than that of the pure PES. It is believed to be due to the fact that a bicontinuous phase morphology exists in the PPS/PES (2 : 8) blends, leading to a lower storage modulus compared with the pure PES having a homogeneous structure. It is noted that microcellular PPS foams exhibit higher storage modulus than the solid PPS. This is because a secondary crystallization takes place during the

high temperature foaming process, leading to a higher crystallinity and hence higher storage modulus.

The loss factor (tanδ) is the ratio of the loss modulus to the storage modulus, and represents the mechanical damping of the viscoelastic system. From the tanδ curves, it can be seen that the PPS/PES blends exhibit two peaks in the glass transition regions of PPS and PES, demonstrating the presence of two phases. The temperature corresponding to the tanδ peak is often regarded as the glass transition temperature, T_g. As can be seen in Figure 13(b), the tanδ peak around 220°C corresponds to the T_g of PES. The presence of PPS decreases the T_g of PES slightly, indicating that the PPS/PES blends are partly miscible. This is in agreement with the DSC results. In addition, an increased PES content leads to a larger area under the tanδ curve, suggesting that the incorporation of PES significantly increases the damping ability of PPS. Microcellular PPS/PES blends exhibit lower glass transition temperatures and internal friction compared with the microcellular PES. However, no clear trend is observed as the PES content increases. As the relationship between the dynamic mechanical properties and the cell morphology of multicomponent blends is very complicated and

there is little relevant literature for reference, additional in-depth research will be the subject of our future work.

CONCLUSIONS

Gaseous mass-transfer and microcellular foaming behaviors of PPS/PES blends have been detailedly investigated using the solid-state batch foaming technique with environment-friendly scCO$_2$ as a physical-blowing agent. The PPS/PES blends with different weight ratios of 10 : 0, 8 : 2, 6 : 4, 5 : 5, 4 : 6, 2 : 8, and 0 : 10 were first prepared through the melt compounding method. The phase morphology, thermal properties, crystallization behavior, and dynamic mechanical properties were found to greatly depend on the blend ratio of the solid PPS/PES blends, which are partly miscible. The addition of PES significantly reduces the crystallinity of PPS phase as the continuity has been destroyed. Gas saturation and desorption studies reveal that the diffusion of CO$_2$ in PPS/PES blends is hindered by the crystal barriers in semi-crystalline PPS component. The equilibrium concentration and desorption diffusivity of CO$_2$ increase as the PES content increases.

Microcellular foams of PPS/PES blends with tailored microstructures can be prepared by adjusting the key factors including blend composition and process conditions such as foaming temperature, foaming time and saturation pressure. The PPS/PES blends show different foaming behaviors at temperatures below and above the melting temperature of PPS. Higher saturation pressure will results in smaller cell size and larger cell density in the microcellular PPS/PES blends due to the higher gas concentration. The mechanisms for the solid-state foaming behaviors of PPS/PES blends with different blend ratios have been illustrated by establishing theoretical models. In addition, it is found that the blend ratio has significant influences on the storage modulus and loss factor for both solid and microcellular PPS/PES blends. The storage modulus of microcellular PPS foams is higher than that of the solid PPS, while the other microcellular PPS/PES blends show lower storage modulus than the solid ones. The results of this study enable the creation of microcellular foamed PPS/PES blends with tailored microstructures and properties for high-performance applications.

ACKNOWLEDGMENTS

REFERENCES

1. Zhao, H. B.; Cui, Z. X.; Sun, X. F.; Turng, L. S.; Peng, X. F. *Ind. Eng. Chem. Res.* **2013**, *52*, 2569.

2. Zhang, R. C.; Xu, Y.; Lu, Z. Y.; Min, M.; Gao, Y.; Huang, Y. G.; Lu, A. *J. Appl. Polym. Sci.* **2008**, *108*, 1829.

3. Díez-Pascual, A. M.; Díez-Vicente, A. L. *ACS Appl. Mater. Interfaces* **2014**, *6*, 10132.

4. Wu, B.; Zheng, X.; Leng, J.; Yang, B.; Chen, X.; He, B. *J. Appl. Polym. Sci.* **2012**, *124*, 325.

5. Wu, X.; Wei, H.; Zhu, J.; Fang, X. *Polym. Plast. Technol. Eng.* **2010**, *49*, 1506.

6. Wu, D.; Wu, L.; Zhang, M.; Zhou, W.; Zhang, Y. *J. Polym. Sci. Part B: Polym. Phys.* **2008**, *46*, 1265.

7. Oyama, H. T.; Matsushita, M.; Furuta, M. *Polym. J.* **2011**, *43*, 991.

8. Lai, M.; Liu, J. *J. Therm. Anal. Calorim.* **2004**, *77*, 935.

9. Shibata, M.; Yosomiya, R.; Jiang, Z.; Yang, Z.; Wang, G.; Ma, R.; Wu, Z. *J. Appl. Polym. Sci.* **1999**, *74*, 1686.

10. Nofar, M.; Park, C. B. *Prog. Polym. Sci.* **2014**, *39*, 1721.

11. Taki, K.; Kitano, D.; Ohshima, M. *Ind. Eng. Chem. Res.* **2011**, *50*, 3247.

12. Ji, G.; Zhai, W.; Lin, D.; Ren, Q.; Zheng, W.; Jung, D. W. *Ind. Eng. Chem. Res.* **2013**, *52*, 6390.

13. Li, J.; Chen, Z.; Wang, X.; Liu, T.; Zhou, Y.; Luo, S. *J. Appl. Polym. Sci.* **2013**, *130*, 4171.

14. Zhi, X.; Zhang, H.; Liao, Y.; Hu, Q.; Gui, C.; Yu, Z. *Carbon* **2015**, *82*, 195.

15. Ling, J.; Zhai, W.; Feng, W.; Shen, B.; Zhang, J.; Zheng, W. G. *ACS Appl. Mater. Interfaces* **2013**, *5*, 2677.

16. Ameli, A.; Nofar, M.; Park, C. B.; Pötschke, P.; Rizvi, G. *Carbon* **2014**, *71*, 206.

17. Famili, M. H. N.; Janani, H.; Enayati, M. S. *J. Appl. Polym. Sci.* **2011**, *119*, 2847.

18. Gong, P.; Ohshima, M. *J. Appl. Polym. Sci.* **2014**, *131*, 39228.

19. Sun, X.; Kharbas, H.; Peng, J.; Turng, L. S. *Polymer* **2015**, *56*, 102.

20. Tan, S. C.; Bai, Z.; Sun, H.; Mark, J. E.; Arnold, F. E.; Lee, C. Y. C. *J. Mater. Sci.* **2003**, *38*, 4013.

21. Miller, D.; Chatchaisucha, P.; Kumar, V. *Polymer* **2009**, *50*, 5576.

22. Dong, G.; Zhao, G.; Guan, Y.; Wang, G.; Wang, X. *J. Appl. Polym. Sci.* **2014**, *131*, 40365.

23. Zhai, W.; Leung, S. N.; Wang, L.; Naguib, H. E.; Park, C. B. *J. Appl. Polym. Sci.* **2010**, *116*, 1994.

24. Ding, J.; Shangguan, J.; Ma, W.; Zhong, Q. *J. Appl. Polym. Sci.* **2013**, *128*, 3639.

25. Gandhi, A.; Asija, N.; Chauhan, H.; Bhatnagar, N. *J. Appl. Polym. Sci.* **2014**, *131*, 40742.

26. Lan, X.; Zhai, W.; Zheng, W. *Ind. Eng. Chem. Res.* **2013**, *52*, 5655.

27. Doroudiani, S.; Park, C. B.; Kortschot, M. T. *Polym. Eng. Sci.* **1998**, *38*, 1205.

28. Luo, Y.; Xin, C.; Yang, Z.; Yan, B.; Li, Z.; Li, X.; He, Y. *J. Appl. Polym. Sci.* **2015**, *132*, 41801.

29. Liu, T.; Zhou, S.; Lei, Y.; Chen, Z.; Wang, X.; Li, J.; Luo, S. *Ind. Eng. Chem. Res.* **2014**, *53*, 19934.

30. Liu, T.; Lei, Y.; Chen, Z.; Wang, X.; Luo, S. *J. Appl. Polym. Sci.* **2015**, *132*, 41443.

31. Javadi, A.; Srithep, Y.; Lee, J.; Pilla, S.; Clemons, C.; Gong, S.; Turng, L. S. *Compos. Part A Appl. S.* **2010**, *41*, 982.

32. Sun, H. L.; Mark, J. E.; Tan, S. C.; Venkatasubramanian, N.; Houtz, M. D.; Arnold, F. E.; Lee, C. Y. C. *Polymer* **2005**, *46*, 6623.

33. Krause, B.; Diekmann, K.; van der Vegt, N. F. A.; Wessling, M. *Macromolecules* **2002**, *35*, 1738.

34. Lee, J. W. S.; Wang, K.; Park, C. B. *Ind. Eng. Chem. Res.* **2005**, *44*, 92.

35. Yang, J.; Huang, L.; Zhang, Y.; Chen, F.; Zhong, M. *J. Appl. Polym. Sci.* **2013**, *130*, 4308.

36. Reglero Ruiz, J. A.; Viot, P.; Dumon, M. *J. Appl. Polym. Sci.* **2010**, *118*, 320.

37. Jacobs, L. J. M.; Kemmere, M. F.; Keurentjes, J. T. F. *Green Chem.* **2008**, *10*, 731.

38. Krause, B.; Mettinkhof, R.; van der Vegt, N. F. A.; Wessling, M. *Macromolecules* **2001**, *34*, 874.

39. Nemoto, T.; Takagi, J.; Ohshima, M. *Polym. Eng. Sci.* **2010**, *50*, 2408.

40. Siripurapu, S.; Gay, Y. J.; Royer, J. R.; DeSimone, J. M.; Spontak, R. J.; Khan, S. A. *Polymer* **2002**, *43*, 5511.

41. Doroudiani, S.; Park, C. B.; Kortschot, M. T. *Polym. Eng. Sci.* **1996**, *36*, 2645.

42. Zhao, Y. F.; Xiao, M.; Wang, S. J.; Ge, X. C.; Meng, Y. Z. *Compos. Sci. Technol.* **2007**, *67*, 2528.

43. Wong, A.; Park, C. B. *Chem. Eng. Sci.* **2012**, *75*, 49.

44. Taki, K.; Nitta, K.; Kihara, S. I.; Ohshima, M. *J. Appl. Polym. Sci.* **2005**, *97*, 1899.

45. Lee, S. T.; Park, C. B.; Ramesh, N. S. Polymeric Foams: Science and Technology. CRC Press: Boca Raton, **2007**; p 64.

46. Liao, X.; Zhang, H.; Wang, Y.; Wu, L.; Li, G. *RSC Adv.* **2014**, *4*, 45109.